

Demodulation of RHESSI count rates by an unbiased linear Bayes estimator

Kaspar Arzner[†]

[†] Paul Scherrer Institut, CH-5232 Villigen PSI, Switzerland
arzner@astro.phys.ethz.ch

Abstract.

The RHESSI experiment uses rotational modulation for x- and gamma ray imaging of solar eruptions. In order to disentangle rotational modulation from intrinsic time variation, an unbiased linear estimator for the spatially integrated photon flux is proposed. The estimator mimics a flat instrumental response under a gaussian prior, with achievable flatness depending on the counting noise. The amount of regularization is primarily given by the modulation-to-Poisson levels of fluctuations, and is only weakly affected by the Bayesian prior. Monte Carlo simulations demonstrate that the mean relative error of the estimator reaches the Poisson limit, and real-data applications are shown.

PACS numbers: 95.55.Ev, 95.55.Ka, 95.75.Wx, 95.75.Pq

1. Introduction

At present, imaging of hard x-rays (HXR) and Gamma rays (GR) is only feasible by selective absorption using different kinds of masks. An elegant and economic variant uses rotation collimators (Schnopper 1968, Willmore 1970, Skinner and Ponman 1995) where a pair of absorbing grids rotates between the true scene and a spatially non-resolving detector (Fig. 1 top). Depending on whether a source is behind or between the grid bars, the observed flux is low or large. As rotation progresses, the true scene becomes thus encoded in a temporal *modulation* of the observed HXR/GR flux (Fig. 1 bottom). In this process, the modulation frequency is not constant but varies with time: glancing passages of the grid bars produce slow modulation, and rippling passages yield fast modulation. The absolute value of the modulation frequency also depends on the offset of the source from the rotation axis, and the modulation amplitude depends on the source size compared to the grid period, in such a way that the amplitude is largest for a point source, and tends to zero if the source size exceeds the grid period. Altogether, this results in a characteristic time series, from which the true scene can be reconstructed by suitable inverse methods (Skinner 1979, Prince et al 1988, Skinner and Ponman 1995, Hurford et al 2002a). While such methods usually assume that the true scene does not depend on time, the present article deals with the complementary

problem of estimating the true *time* dependence of the (spatially integrated) scene, and distinguishing it from rotation modulation. This is called here the ‘*demodulation*’ problem.

The data which we envisage are obtained by the Reuven Ramaty High-Energy Solar Spectroscopic Imager (RHESSI, Lin et al 2002; Zehnder et al 2003). This solar-dedicated space mission uses rotation modulation for HXR/GR imaging of solar eruptions. The RHESSI instrument has 9 pairs of aligned HXR/GR-absorbing grids (9 ‘subcollimators’) which are fixed on the rotating spacecraft. Different subcollimators have different grid spacings, which produce sinusoidal spatial transmission patterns (see Section 2 for details). Behind each subcollimator there is a germanium detector which records the arrival time and energy (3 keV - 17 MeV) of the incoming HXR/GR photons. From a statistical point of view, the photon arrival times form a Poisson process with non-constant intensity. The change in intensity is due to rotation modulation, but may also have contributions from the time dependence of the true scene.

The latter is highly interesting from a solar physics point of view, because it is related to particle acceleration in impulsive solar eruptions. The existence of temporal fluctuations of the true HXR scene down to time scales of hundred milliseconds has been confirmed by earlier observations (Dennis 1985, Machado et al 1993, Aschwanden et al 1993). However, these time scales interfere with the RHESSI rotation modulation which occurs on time scales of milliseconds to seconds. In order to disentangle time dependence of the true scene from rotation modulation the RHESSI data must be demodulated. The most general outcome of this process would be the true scene as a function of both space and time. But the information contained in the photon counts is rather limited, and must be shared between spatial and temporal degrees of freedom of the true scene. We therefore restrict ourselves here to the simpler problem of estimating the spatially integrated true scene as a function of time. The motivation for this stems also from the wish to compare RHESSI HXR data with spatially integrated broadband radio observations. Both types of radiation are emitted by electrons of comparable energy, and there is some controversy in the field whether or not the two populations actually agree. The actual radio observations have a time resolution of 100 milliseconds, and collect radiation from the whole sun.

The demodulation of RHESSI data is, in general, an inverse problem. Temporal and spatial variations of the true scene are entangled by the observation method. An exception only arises if the time scale of interest exceeds the RHESSI rotation period $T_S \simeq 4\text{s}$, so that demodulation can be replaced by a running average over T_S . Otherwise, a good estimator for the spatially integrated scene requires some a priori information on its spatial structure in order to outweigh or damp the rotational modulation. Such information may either come from independent observations, or from RHESSI itself. In the latter case, one may use standard RHESSI imaging techniques (Hurford et al 2002a) to obtain an estimate of the time-averaged true scene. These techniques assume that the true scene is independent of time. Under this assumption, the true scene can be estimated after half a spacecraft rotation, when all possible grid orientations are cycled,

and higher-quality results arise from multiples of $T_S/2$.

The aim of the present paper is to resolve time scales $\ll T_S/2$. We do not attempt here a fully general solution where the spatially true integrated scene is found at each point of time. Instead, we will assume that the true scene can be considered as piecewise constant during time intervals τ of order of 100 ms. Such intervals are shorter than most previously reported time scales, and they also agree with the time resolution of the comparative radio observations mentioned above. The present article describes an efficient linear estimator for the spatially- and τ -integrated scene. The construction of the estimator follows the lines of classical Wiener filtering (Rybicki and Press 1992), but operates in time (not frequency) space.

The paper is organized as follows. Section 2 summarizes some relevant technicalities of the RHESSI instrument. Section 3 presents our inverse theory approach including counting statistics (Sect. 3.1) and a priori information (Sect. 3.2). The resulting estimator is then discussed in Sections 4.1 - 4.3, and its performance (Sect. 4.4) and robustness against violation of the prior assumptions (Sect. 4.5) are explored by Monte Carlo simulations. Section 4.6 shows the algorithm at work on real data from a solar eruption. See Tab. 1 for an overview of notation.

$B(\mathbf{x}, t)$	true scene [ct asec ⁻² s ⁻¹]
T_S	RHESSI spin period [s]
τ	time interval [s] to be estimated
$\mu = (i, j)$	multi-index for (subcollimator, time)
$M_i(\mathbf{x}, t)$	modulation pattern
Δ_μ	time bin [s]
λ_μ	expected counts in Δ_μ [ct]
c_μ	observed counts in Δ_μ [ct]
b	expected counts in τ [ct]
\hat{b}	$= w_\mu c_\mu$, estimator for b [ct]

Table 1. Notation. Angular position $\mathbf{x} = (x, y)$ is measured in locally Cartesian heliocentric coordinates, and the dependence on \mathbf{x} is therefore also termed ‘spatial’. One arc second (1”) corresponds to 700 km on the solar disc.

2. The RHESSI instrument

We start with a brief description of the RHESSI response to HXRs and GRs, which defines the ‘forward’ problem of converting the true scene into the observed counts. We shall only consider photons out of a fixed energy band, average all energy-dependent quantities over that energy band, and omit the energy dependence in the notation.

2.1. Modulation patterns

The instantaneous transmission probabilities of RHESSI's subcollimators, as a function of photon incidence direction, are called the modulation patterns. They may be visualized as the grids' shadow on the sky plane if the detectors were operated in a transmitting mode. When expressed in terms of heliocentric cartesian coordinates $\mathbf{x} = (x, y)$ (over the limited RHESSI field of view, cartesian and angular coordinates are equivalent), the modulation patterns can be approximated by

$$M_i(\mathbf{x}, t) = a_{0i}(t) + a_{1i}(t) \cos \left(\mathbf{k}_i(t) \cdot (\mathbf{x} - \mathbf{P}(t)) + \Psi_i(t) \right). \quad (1)$$

Above, the $\mathbf{k}_i(t)$, $i = 1..9$, are the grid vectors which rotate clockwise with the spacecraft rotation period T_S . All grid periods ($2\pi/|k^i| = 2.6 \cdot 3^{i/2}$ asec) are small compared to the solar diameter ($1920''$) and to the fields of view of the individual subcollimators ($3600'' \dots 27.000''$). The coefficients ($a_{ni}(t), \Psi_i(t)$) describe the internal shadowing of the grids; they depend on photon energy and only weakly on time as long as the source is in the central part of the field of view, which is the case for solar sources. The vector $\mathbf{P}(t)$ is the imaging (optical) axis. It generally varies with time, since it is not aligned with the rotation axis, which, in turn, may differ from the inertial axis. As a consequence, $\mathbf{P}(t)$ traces out a relatively complicated orbit on the solar disc, which is continuously monitored by the onboard aspect systems (Fivian et al 2002, Hurford et al 2002b), and the details of which need not concern us here. All vectors \mathbf{x} , $\mathbf{k}(t)$ and $\mathbf{P}(t)$ ly in the solar plane.

2.2. Onboard data reduction

In order to avoid detector and telemetry saturation, mechanical attenuators can be inserted into the optical path, and photon counts can be decimated by a clocked veto: during one binary microsecond ($1b\mu s = 2^{-20}s$), all events are accepted, during the next $(N_d - 1)b\mu s$, they are all rejected. Both reduction methods preserve the statistical independence of the photon arriving times, and can be absorbed in the definition of the modulation patterns.

2.3. Observational artifacts

While Equation (1) represents the ideal instrumental response, the real observations suffer from several non-idealities such as detector saturation at high count rates, and sporadic breakdown of the whole detection chain. The latter is presumably caused by cosmic rays (Smith et al 2002); the resulting data gaps occur at random about once per second, and have durations of milliseconds to seconds (see Fig. 1 bottom for an example). All non-idealities are combined on-ground in livetime measures $0 \leq L_i(t) \leq 1$, which estimate the operational fraction of each detector in a given time bin. The effect of livetime is taken into account by multiplying the modulation patterns $M_i(\mathbf{x}, t)$ by $L_i(t)$. Times with $L < 0.3$ are discarded, which prevents detector saturation and redundant or undefined ($L = 0$) numerical operations.

3. Inverse Method

3.1. Principle and treatment of measurement errors

Let $B(\mathbf{x}, t)$ denote the solar brightness distribution at position \mathbf{x} and time t , and let the RHESSI counts be grouped in time bins $\Delta_\mu \in \tau$ where $\mu = (i, j)$ labels subcollimator and time. The set $\{\mu\}$ may comprise all or only some of the 9 subcollimators, and different subcollimators may have different time bins. The observed counts c_μ in different bins Δ_μ are supposed to be statistically independent Poisson variates with expectation values

$$\lambda_\mu = \int_{\Delta_\mu} dt \int d\mathbf{x} M_{i(\mu)}(\mathbf{x}, t) B(\mathbf{x}, t), \quad (2)$$

where we have written $i(\mu)$ to extract the subcollimator index out of μ . Non-solar background is neglected. The goal is to estimate spatially integrated true scene

$$b = \int_\tau dt \int d\mathbf{x} B(\mathbf{x}, t) \quad (3)$$

in the time interval τ , as would be observed in the absence of the subcollimators ($M_i(\mathbf{x}, t) = 1$). The estimator \hat{b} for b is searched in the linear form

$$\hat{b} = w_\mu c_\mu \quad (\text{summation convention}). \quad (4)$$

In the sequel we shall choose w_μ to make \hat{b} efficient, i.e., unbiased and minimum-variance among all unbiased estimators. To this end, and for the sake of a concise notation, we first introduce the expectation operator \mathcal{E} of a general function $X(b, \mathbf{c})$ of the true b and of the observed counts $\mathbf{c} = \{c_\mu\}$. This is done within a Bayesian framework where each true scene B has assigned a prior probability $P(B)$, so that $P(\mathbf{c}, B) = P(\mathbf{c}|B)P(B)$. One thus has

$$\mathcal{E}X(b, \mathbf{c}) = \underbrace{\int dP(B)}_{\mathcal{E}_B} \underbrace{\sum_{\mathbf{c}=0}^{\infty} \prod_{\mu} \frac{e^{-\lambda_\mu} \lambda_\mu^{c_\mu}}{c_\mu!}}_{\mathcal{E}_{\mathbf{c}|B}} X(b, \mathbf{c}) \quad (5)$$

where λ_μ and b depend on B according to Equations (2) and (3). The expectation operator (5) involves an average over the counting statistics, followed by an average over the prior scenes, and we write $\mathcal{E} = \mathcal{E}_B \mathcal{E}_{\mathbf{c}|B}$ to stress this sequence. If a quantity X is independent of the observed counts \mathbf{c} then \mathcal{E} reduces to \mathcal{E}_B .

So far, \mathcal{E}_B is still a formal object. Let us accept this for the moment, and proceed with the design of the weights $\mathbf{w} = \{w_\mu\}$. A first natural request is that the estimator (4) is unbiased, $\mathcal{E}(\hat{b}) = \mathcal{E}(b)$, requiring that

$$w_\mu \mathcal{E}_B(\lambda_\mu) = \mathcal{E}_B(b). \quad (6)$$

This condition locates \mathbf{w} along the direction of $\mathcal{E}_B(\boldsymbol{\lambda})$. In order to find a unique solution \mathbf{w} we additionally require the variance $\mathcal{E}(\hat{b} - b)^2$ to be minimal, and verify a posteriori that this condition is sufficient to ensure uniqueness of the

solution. Unbiasedness and minimum-variance constraints are combined by minimizing $\mathcal{E}(\hat{b}-b)^2 + \zeta \mathcal{E}(\hat{b}-b)$ with respect to \mathbf{w} , where the Lagrange multiplier ζ must be adjusted to fulfill Equation (6). The resulting minimum condition is

$$\mathcal{E}(c_\mu c_\nu)w_\nu - \mathcal{E}(bc_\nu) + \zeta \mathcal{E}(c_\nu) = 0, \quad (7)$$

or, after performing the average $\mathcal{E}_{\text{c|B}}$ over counting statistics,

$$\mathcal{E}_{\text{B}}(\lambda_\mu \lambda_\nu + \lambda_\mu \delta_{\mu\nu})w_\nu - \mathcal{E}_{\text{B}}(b\lambda_\nu) + \zeta \mathcal{E}_{\text{B}}(\lambda_\nu) = 0. \quad (8)$$

Here it was used that $\mathcal{E}_{\text{c|B}}(c_\mu c_\nu) = \lambda_\mu \lambda_\nu + \lambda_\mu \delta_{\mu\nu}$ for independent counts c_μ . One may now see that Equation (8) has indeed a unique solution \mathbf{w} if only $\lambda_\mu > 0$. Under this condition, the matrix $\Lambda_{\mu\nu} = \lambda_\mu \lambda_\nu + \lambda_\mu \delta_{\mu\nu}$ is strictly positive definite: $(\mathbf{x}, \Lambda \mathbf{x}) = (\mathbf{x} \cdot \boldsymbol{\lambda})^2 + \sum_\mu \lambda_\mu x_\mu^2 > 0$ for all $\mathbf{x} \neq \mathbf{0}$. Since the prior average \mathcal{E}_{B} represents a sum of positively weighted Λ 's, the matrix $\mathcal{E}_{\text{B}}\Lambda$ is also positive definite and therefore invertible – indeed, the condition number of $\mathcal{E}_{\text{B}}\Lambda$ can not exceed the condition number of Λ ‡.

Let us add at this point an interpretation of the matrix Λ . For any fixed realization of the true scene B , the fluctuations of the observed counts c_μ have two causes: instrumental modulation and counting noise. These two causes give rise to the two contributions $\lambda_\mu \lambda_\nu$ and $\lambda_\mu \delta_{\mu\nu}$ in the matrix $\Lambda_{\mu\nu}$. At large count rates ($\lambda_\mu \gg 1$), $\Lambda_{\mu\nu}$ is dominated by $\lambda_\mu \lambda_\nu$, and at small count rates ($\lambda_\mu < 1$) it is dominated by $\lambda_\mu \delta_{\mu\nu}$. The condition number of $\Lambda_{\mu\nu}$ increases with increasing count rates and is bounded from above by $(|\boldsymbol{\lambda}|^2 + \max(\lambda_\mu)) / \min(\lambda_\mu)$ ‡. Thus, higher count rates allow weaker-conditioned $\Lambda_{\mu\nu}$. We may interpret this by saying that the counting noise regularizes the problem of inverting modulation, and that the amount of regularization is given by the level of Poisson fluctuations compared to the modulation amplitude.

3.2. Choice of the prior

We turn now to the definition of \mathcal{E}_{B} (Eq. 5). Formally, the true brightness distribution $B(\mathbf{x}, t)$ is an element of a function space, and its a priori probability measure $dP(B)$ is a functional. In order to avoid technical complications while retaining the basic probabilistic features, we make the following simplifying assumptions: the true brightness distribution $B(\mathbf{x}, t)$ is concentrated in a (known) spatial prior, where it may have (unknown) substructures which do not vary significantly during the time interval τ for which the unmodulated counts are to be estimated. Thus $B(\mathbf{x}, t) \simeq B(\mathbf{x})$ for $t \in \tau$. Now we recall that $B(\mathbf{x})$ enters the problem only upon weighting with the modulation patterns (Eq. 2). Therefore the detailed structure of $B(\mathbf{x})$ on scales which are small compared to the period of the modulation patterns do not matter, and we may represent $B(\mathbf{x})$ by a (finite) collection of point sources

$$B(\mathbf{x}) = \sum_k B_k \delta(\mathbf{x} - \mathbf{x}_k) \quad (9)$$

‡ see Appendix

with the agreement that $B_k > 0$ and that the spacing between the \mathbf{x}_k is not less than the finest resolvable scale $l_0 \sim \min(|\mathbf{k}_i|^{-1})$. Since we do not wish to introduce any bias into the brightness distribution, except for its localization in the prior region, we set $dP(B) = \prod_k \xi(\mathbf{x}_k) d\mathbf{x}_k$ where $\xi(\mathbf{x})$ is a pdf concentrated in the prior region. This definition of $dP(B)$ is insensitive to the amplitude of B but sensitive to its support. Applying \mathcal{E}_B reduces now to an elementary calculation, and Equation (8) becomes

$$\left[(1 - \gamma) \langle M_\mu M_\nu \rangle + \gamma \langle M_\mu \rangle \langle M_\nu \rangle + \beta^{-1} \langle M_\mu \rangle \delta_{\mu\nu} \right] w_\nu = (\tau - \zeta \beta^{-1}) \langle M_\mu \rangle \quad (10)$$

with

$$\langle M_\mu \rangle = \int_{\Delta_\mu} dt \int d\mathbf{x} \xi(\mathbf{x}) M_{i(\mu)}(\mathbf{x}, t) \quad (11)$$

$$\langle M_\mu M_\nu \rangle = \int_{\Delta_\mu} dt \int_{\Delta_{t\nu}} dt' \int d\mathbf{x} \xi(\mathbf{x}) M_{i(\mu)}(\mathbf{x}, t) M_{i(\nu)}(\mathbf{x}, t') \quad (12)$$

$$\beta = \sum_n B_n \quad (13)$$

$$\gamma = 1 - \beta^{-2} \sum_n B_n^2. \quad (14)$$

Equation (10) is our main result. The parameter $0 \leq \gamma < 1$ is a ‘filling factor’: $\gamma = 0$ corresponds to a single unresolved source, whereas $\gamma \rightarrow 1$ stands for a prior region densely covered with sources. If the diameter of the prior region exceeds the angular pitch, then $\gamma \rightarrow 1$ indicates the loss of modulation, while $\gamma = 0$ retains full modulation, yet at an unknown phase. Note that β is the quantity which actually is to be estimated. Its occurrence in Equation (10) is, however, unproblematic. On the right hand side, β is absorbed in the Lagrange multiplier ζ . On the left hand side, β occurs in the regularization only, where it may be replaced by a simpler estimate \hat{b}_0 (Sect. 4.1) without qualitatively changing the solution. Since ζ only affects the scaling of the right hand side vector in Equation (10), its adjustment for unbiasedness (Eq. 6) is equivalent to re-scaling $\mathbf{w} \rightarrow \mathbf{w} \tau (\mathbf{w} \cdot \langle \mathbf{M} \rangle)^{-1}$, which is easily implemented numerically.

It remains to select the pdf $\xi(\mathbf{x})$. Our choice is largely ad hoc, and must be justified by demonstrating that the resulting estimator \hat{b} remains efficient and well-behaved even if the prior assumptions are violated. This will be done in Sections 4.4 and 4.5. Here we qualitatively motivate our choice. First of all, $\xi(\mathbf{x})$ should be simple and depend on not more than a few parameters in order to facilitate operational data processing. One set of parameters which is provided by the RHESSI data products is the centroid \mathbf{x}_0 of the HXR emission derived from time-integrated ($\gg \tau$) RHESSI imaging. It is natural to center $\xi(\mathbf{x})$ on \mathbf{x}_0 . In addition to the centroid we would like to specify the rough size l of the prior region, but not any of its details, since these are not known on time scales as small as τ . The choice of l reflects the uncertainty of the true scene, and may be based on RHESSI imaging or on independent observations. In particular, we may chose l such as to cover a solar ‘active region’ (Howard 1996) derived from magnetic field observations.

In any case, l should not be unrealistically small; simulations (Sect. 4.5) suggest that $l > 10''$ is a reasonable, conservative, choice. Owing to the inherent rotation symmetry of the rotation modulation observing principle, it is suggestive to choose an isotropic form for $\xi(\mathbf{x})$, although this is by no means a rigorous request. From a practical point of view it is also important that the integrals in Equation (11) and (12) can be performed analytically as far as possible to save numerical operations. A choice which fulfills the above criteria is

$$\xi(\mathbf{x}) = (2\pi l^2)^{-1} e^{-(\mathbf{x}-\mathbf{x}_0)^2/2l^2}. \quad (15)$$

Since the coefficients $a_{ni}(t)$ and $\Psi_i(t)$ in Equation (1) are slowly varying with time, they may be replaced by discrete-time versions $a_{n\nu}$ and Ψ_ν . Equations (11, 12) then become

$$\langle M_\mu \rangle = \sum_{m=0}^1 a_{m\mu} e^{-\frac{l^2}{2}|m\mathbf{k}_{i(\mu)}|^2} \int_{\Delta_\mu} dt \cos(m\phi_\mu(t)) \quad (16)$$

$$\begin{aligned} \langle M_\mu M_\nu \rangle &= \sum_{s=\pm 1} \sum_{m,n=0}^1 \frac{a_{m\mu} a_{n\nu}}{2} e^{-\frac{l^2}{2}(|m\mathbf{k}_{i(\mu)}|^2 + |n\mathbf{k}_{i(\nu)}|^2)} \int_{\Delta_\mu} dt \int_{\Delta_\nu} dt' \times \\ &\times e^{-l^2 s m n \mathbf{k}_{i(\mu)}(t) \cdot \mathbf{k}_{i(\nu)}(t')} \cos(m\phi_\mu(t) + s n \phi_\nu(t')) \end{aligned} \quad (17)$$

with $\phi_\mu(t) = \mathbf{k}_{i(\mu)}(t) \cdot (\mathbf{x}_0 - \mathbf{P}(t)) + \Psi_\mu$. On time scales $\tau \ll T_S/2$, mostly terms with $s=-1$ contribute to Equation (17). The time integrals in Equations (16) and (17), which depend on the actual spacecraft motion, are evaluated numerically.

3.3. Choice of time bins

RHESSI detects individual photons, and their assignment to time bins is an important first step of the demodulation procedure. There are two, potentially conflicting, requests on the time bins Δ_μ . On the one hand, Δ_μ should resolve (say, by a factor 10) the instantaneous modulation period

$$\tau_i^{\text{mod}}(t) \sim T_S |\mathbf{k}_i(t) \times (\mathbf{x}_0 - \mathbf{P}(t))|^{-1} \quad [s] \quad (18)$$

of a source at position \mathbf{x}_0 . On the other hand, demodulation is only beneficial if there are sufficient counts to observe modulation against Poisson noise. This requires, empirically, some 5 counts per time bin. In addition, the time bins should be integer fractions of τ in order to minimize roundoff error. We therefore adopt the following rule:

$$\Delta_\mu = \frac{\tau}{1 + \text{round}(\Delta_\mu^*/\tau)}, \quad \Delta_\mu^* = \max\left(\frac{5}{\langle c_{i(\mu)} \rangle}, \frac{1}{10} \min_{t \in \tau} \tau_{i(\mu)}^{\text{mod}}(t)\right) \quad (19)$$

where $\langle c_i \rangle$ is the average count rate [ct/s] in subcollimator i . The factors 5 and 10 in Equation (19) are empirical.

3.4. Numerical implementation

Equations (16) and (17) are evaluated by an extended trapezoidal rule with intermediate step size adapted to the modulation frequency and amplitude. The inversion of the matrix on the left hand side of Equation (10) is performed by singular value decomposition (Golub and Van Loan 1989) with explicit control of condition number.

4. Discussion

4.1. Limiting behaviour

Let us start our discussion by verifying that the estimator (4) remains well-behaved and meaningful in extreme cases where the prior is pointlike or flat, and where the observed flux tends to zero. The limit of infinite flux is discussed in Sect. 4.2.

At very low count rates ($\ll 1 \text{ ct}/\tau_i^{\text{mod}}$), modulation is no longer observable, and one may thus expect that \hat{b} should reduce to a simple average, which is an efficient estimator for the pure counting noise problem. Indeed, in the limit $\beta \rightarrow 0$, Equation (10) yields (after adjusting ζ to satisfy Eq. 6)

$$\hat{b} \rightarrow \hat{b}_0 \doteq \frac{\tau \sum_{\mu} c_{\mu}}{\sum_{\mu} \langle M_{\mu} \rangle} \simeq \frac{\tau \sum_{\mu} c_{\mu}}{\sum_{\mu} \Delta_{\mu} a_{0\mu}}. \quad (20)$$

Equation (20) will be referred to as ‘uniform average’ since it involves uniform weights ($w_{\mu} = \text{const}$). The last approximation in Equation (20) holds if the modulation is fast ($\tau_i^{\text{mod}} \ll \tau$) or weak ($|\mathbf{k}_i|l \gg 1$), so that the term with $m=1$ in Equation (16) can be neglected. The uniform average \hat{b}_0 provides a simple guess of b , which is - hopefully - improved by the more sophisticated estimator (4). We shall see in Sect. 4.4 - 4.5 that this is in fact the case.

The uniform average (20) is also attained if $l = 0$ or $\gamma = 1$, both representing deterministic limits with completely localized or densely filled prior regions. In either case, the term $(1 - \gamma)\langle M_{\mu}M_{\nu} \rangle + \gamma\langle M_{\mu} \rangle\langle M_{\nu} \rangle$ reduces to $\langle M_{\mu} \rangle\langle M_{\nu} \rangle$, so that Equation (10) has the solution $w_{\mu} = \text{const}$, and \hat{b} reduces to \hat{b}_0 .

Another situation of interest is $l \rightarrow \infty$ where the prior becomes globally flat. For $l \rightarrow \infty$ one can derive from Equations (16-17) that $\langle M_{\mu} \rangle \rightarrow a_{0\mu}\Delta_{\mu}$ and $\langle M_{\mu}M_{\nu} \rangle \rightarrow a_{0\mu}\Delta_{\mu}a_{0\nu}\Delta_{\nu} + \frac{1}{4}(a_{1\mu}\Delta_{\mu})^2\delta_{\mu\nu}$. Thus Equation (10) can be inverted by the Sherman-Morrison formula (Press et al 1998), and one finds (after adjusting ζ)

$$\hat{b} \rightarrow \hat{b}_{\text{fl}} \doteq \frac{\tau \sum_{\mu} c_{\mu} \sigma_{\mu}^{-2}}{\sum_{\mu} \Delta_{\mu} a_{0\mu} \sigma_{\mu}^{-2}} \quad \text{where} \quad \sigma_{\mu}^2 = 1 + \frac{1}{4}(1 - \gamma)\beta\Delta_{\mu} \frac{a_{1\mu}^2}{a_{0\mu}}. \quad (21)$$

From Equation (21) the uniform average (20) is recovered if $\frac{1}{4}(1 - \gamma)\beta\Delta_{\mu} \frac{a_{1\mu}^2}{a_{0\mu}} \ll 1$. Otherwise a correction arises which weakly varies with time (Sect. 2). Bins with large modulation amplitude $a_{1\mu}$ are given less weight in Equation (21), which is reasonable since their uncertainty is larger.

In summary, we have found that the estimator (4) has well-defined and meaningful analytic limits when the flux tends to zero ($\beta \rightarrow 0$), and when the prior is completely restrictive ($l \rightarrow 0$) or completely nonrestrictive ($l \rightarrow \infty$).

4.2. Geometrical interpretation

In the limit of infinite count rates, the counting noise becomes unimportant and Equation (10) admits a purely geometrical interpretation. Recalling the assumption $B(\mathbf{x}, t) \simeq B(\mathbf{x})$ for $t \in \tau$, one has that $\mathcal{E}_{\text{c|B}}(b) = \int d\mathbf{x} B(\mathbf{x}) \Phi(\mathbf{x})$ with $\Phi(x) \doteq w_\mu M_\mu(\mathbf{x})$ and $M_\mu(\mathbf{x}) \doteq \int_{\Delta_\mu} dt M_{i(\mu)}(\mathbf{x}, t)$. Therefore $\mathcal{E}_{\text{c|B}}(b)$ is a good estimator for b for *arbitrary* $B(\mathbf{x})$ if $\Phi(\mathbf{x})$ is independent of \mathbf{x} . The modulation patterns would then be canceled. However, the functions $M_\mu(\mathbf{x})$ are neither orthogonal nor complete, so that $\Phi(\mathbf{x})$ cannot be made constant by whatever choice of weights w_μ . Instead, we may try to minimize the fluctuations of $\Phi(\mathbf{x})$ within the spatial prior $\xi(\mathbf{x})$, and therefore minimize $\int \xi(\mathbf{x})(\Phi(\mathbf{x}) - \text{const})^2 d\mathbf{x}$. This yields $\langle M_\mu M_\nu \rangle w_\nu \propto \langle M_\mu \rangle$. Comparing this expression to Equation (10) we see that Equation (10) minimizes the fluctuations of $\Phi(\mathbf{x})$ within the spatial prior under the maximum-modulating assumption that there is a single point source ($\gamma = 1$) observed at infinite count rate ($\beta \rightarrow \infty$).

The matrix $\mathbf{M} = \langle M_\mu M_\nu \rangle$ is generally ill-conditioned, and the weights $\mathbf{w} = \mathbf{M}^{-1} \langle \mathbf{M} \rangle$ therefore oscillate. At finite count rate, the excursions to large $|w_\mu|$ amplify the Poisson noise, and thereby impair the estimator \hat{b} (Eq. 4). An optimum estimator must thus limit the oscillations of \mathbf{w} to a level which commensurates with the Poisson noise. Equation (10) provides a possible trade-off.

Fig. 2 illustrates the resulting function $\Phi(\mathbf{x})$ for $\gamma = 0$ and different β , using aspect data of February 26 2004, subcollimators (3,4,5,6), and $\tau = 0.2$ s. The time bins Δ_μ are (2.8, 4.8, 8.5, 15)ms, and the spatial prior (size $l = 40''$) is centered at the source position (245'', 340'') estimated from time-integrated RHESSI imaging. The black mask in Fig. 2 indicates the 10% level of the spatial prior (Eq. 15). In order to assess the constancy of $\Phi(\mathbf{x})$ we consider the standard deviation $\Delta\Phi$ and mean Φ inside the black mask. In a noiseless world ($\beta \rightarrow \infty$), the modulation patterns would admit $\Delta\Phi/\langle\Phi\rangle \sim 0.0058$ (Fig. 2a). Taking the actual counting noise ($\beta \sim \hat{b}_0 = 6200$ ct/s) into account, $\Delta\Phi/\langle\Phi\rangle \sim 0.024$ is still achievable (Fig. 2b). For comparison, the uniformly weighted ($w_\mu = \text{const}$) case is also shown (Fig. 2b, $\Delta\Phi/\langle\Phi\rangle \sim 0.14$), which corresponds to the limit $\beta \rightarrow 0$. As can be seen, the function $\Phi(\mathbf{x})$ becomes less efficient in canceling the modulation patterns when the count rate β decreases. But, at the same time, the sensitivity of \hat{b} to Poisson noise increases. The trade-off chosen by the present method is shown in Fig. 2b.

4.3. Weighting mechanism

In a generic situation ($\gamma \neq 1$, $l \neq 0$, $\hat{b}_0 \gg 1$) one may identify three mechanisms by which the weights operate. These are most easily discussed in terms of Fourier modes of the modulation. First, if the modulation phase is resolved ($|\mathbf{k}_i|l \ll 1$) then modulation

can ‘actively’ be countersteered. Secondly, if the modulation phase is not resolved but the instantaneous modulation frequency $1/\tau_i^{\text{mod}}$ (Eq. 18) is known, then counts with $\tau_i^{\text{mod}} \ll \tau$ can be suppressed because they do not allow a ‘passive’ averaging. This suppression works for each subcollimator individually. (Although τ_i^{mod} does not explicitly show up in Equation (10), it is implicitly contained in the diagonal blocks of correlation function $\langle M_\mu M_\nu \rangle$, see Fig. 4 below). Thirdly, the matrix $\langle M_\mu M_\nu \rangle$ couples different subcollimators, which regulates the relative weighting of different subcollimators.

The different mechanisms are illustrated in Figures 3 and 4, showing simulated data of subcollimators (4,5,6,7) with $\mathbf{x}_0 = (885'', 161'')$, $l = 20''$, $\gamma = 0.2$, and a single intense ($\sim 3 \times 10^4$ ct/s/subcollimator) point source located at \mathbf{x}_0 . The chosen geometry represents a solar limb source. The simulated counts are divided into disjoint intervals of duration $\tau = 0.25$ s (Fig. 3), and time bins are equal ($\Delta_\mu = 0.0025$ s) for better comparability. The outweighing of modulation is most clearly seen in the coarsest subcollimator (Fig. 3, #7) with $l/p_7 = 0.16$, where $p_7 = 2\pi/|\mathbf{k}_7| = 122''$ is the period of subcollimator #7. The modulation is also – though less efficiently – outweighed in subcollimator #6 ($l/p_6 = 0.28$), while the finest subcollimators #5 ($l/p_5 = 0.49$) and #4 ($l/p_4 = 0.85$) mostly operate in an averaging mode, with priods of low τ_{mod}^i being suppressed.

The different regimes manifest in different forms of the correlation $\langle M_\mu M_\nu \rangle$ (Fig. 4). For $l/p_i \ll 1$ the matrix $\langle M_\mu M_\nu \rangle$ approximately factorizes into $\langle M_\mu \rangle \langle M_\nu \rangle$ (Fig. 4, #7). With increasing l/p_i , the autocorrelation of a single subcollimator takes the form $\langle M_{(i,t)} M_{(i,t')} \rangle \sim \cos(2\pi \frac{t-t'}{\tau_i^{\text{mod}}}) e^{-(t-t')^2/2(\tau_i^{\text{d}})^2}$ with decay time $\tau_i^{\text{d}} \sim (lk_i)^{-1}(\dot{\mathbf{k}}_i \cdot \mathbf{x}_0)^{-1}$ (Eq. 17). Here, both τ_i^{d} and τ_i^{mod} depend to first order on $(t+t')/2$, which results in the ‘chirping’ behaviour of Fig. 4, subcollimator #4. The chirp towards low modulation frequencies is associated with a drop of the corresponding weights (Fig. 3 top, time interval in dashed lines).

4.4. Performance

The quality of the demodulation and its robustness against violation of prior assumptions have been explored by Monte Carlo simulations. Figure 5 shows, as an example, the relative errors $|b - \hat{b}|/b$ of 10^5 simulated time intervals τ , together with uniform values $|b - \hat{b}_0|/b$ and the relative Poisson error $N_{\text{tot}}^{-1/2}$ with N_{tot} the total number of counts in τ . Dots illustrate a subsample of the simulation; graphs represent the full ensemble averages. The spatial prior is centered at $\mathbf{x}_0 = (420'', -630'')$ and has size $l = 40''$. The simulated brightness distribution is a superposition of 10 random sources $A_s \exp\{-\frac{1}{2}(t - t_s)^2/\tau_s^2 - \frac{1}{2}(\mathbf{x} - \mathbf{x}_s)^2/l_s^2\}$ with uniform relative amplitudes $A_s/\sum_s A_s$, Gaussian positions \mathbf{x}_s (mean \mathbf{x}_0 , variance $l^2/4$), uniform sizes $l_s \in (1'' \dots 5'')$, and uniform intrinsic time scales $\tau_s \in (0.2\text{s} \dots 1\text{s})$. The assumed filling factor is $\gamma = 0.2$, whereas the true value scatters from 0.8 to 0.9. Data gaps are neglected. At low count rates, the error is dominated by the Poisson noise, and all three types of error coincide. At higher

count rates, the error becomes dominated by modulation, and the uniform average no longer improves with improving counting statistics. The estimator \hat{b} performs better, and reaches the Poisson limit for integration times $\tau \geq 8\text{ms}$ and count rates up to 10^5 ct/s/subcollimator. The latter is, in fact, the practically relevant range – higher count rates do not occur because the RHESSI detectors need $\lesssim 8 \times 10^{-6}\text{s}$ to recover after each photon impact. One may thus be confident that – at least with regard to the (tolerant) error measure $\mathcal{E}(|b - \hat{b}|/b)$ – the estimator \hat{b} works optimally for practical purposes. The degradation of $|b - \hat{b}|/b$ at highest count rates and largest τ is attributed to the increased susceptibility to prior assumptions, and possibly also to numerical errors as the involved matrices become large and weak-conditioned. (Condition numbers up to 10^5 occur at 10^6 ct/s/subcollimator.) Extended simulations including different brightness distributions, data gaps, and γ values yielded similar results.

4.5. Influence of the prior

An important practical feature of Bayesian inverse methods is their robustness against violation of the prior assumptions. If a wrong prior is used, then the result will be degraded but it should not become (much) worse than if no prior was used at all (i.e., if the weights were uniform or the prior was flat, $l \rightarrow \infty$). We shall now demonstrate that this goal is met by our demodulation method. Figure 6 shows simulations performed at fixed count rate of $2 \cdot 10^4$ ct/s/subcollimator and fixed integration time $\tau = 0.12\text{s}$, but with varying size l of the prior region, and with different offsets between the true and prior centroids. In each simulation, a prior centroid \mathbf{x}_0 is chosen at random across the solar disc, and the true centroid is placed d arc seconds away in random direction. The true source has several gaussian components, which are all concentrated in a narrow ($3''$) region around the true centroid. The simulated imaging axis $\mathbf{P}(t)$ moves within the central ($<200''$) region of the solar disc. While the cases $d = (0, 10, 50)''$ reflect realistic uncertainties of RHESSI observations, $50''$ being a conservative value, the case $d = 500''$ is overly pessimistic and is included here for demonstration purposes. The relative errors (vertical axis) are defined as in Figure 5; the ‘flat prior’ estimator is given by Equation (21). Dots again represent a subsample of the simulation, while curves represent averages over the full sample ($6 \cdot 10^4$).

If the prior centroid coincides with the true one ($d=0''$, black solid line), then the demodulation reaches the Poisson limit for $l \lesssim 5''$, i.e., as long as the prior width does not exceed the true width by more than a factor $\lesssim 2$. If the true and assumed centroids differ ($d > 0$), then the demodulation does no longer reach the Poisson limit, and degradation depends on the ratio d/l . As can be seen, all error curves collapse to the optimum ($d = 0$) one when $l \gtrsim d$, indicating that discrepancies between true and prior centroids are tolerated up to the size of the prior region. Except for very large and unrecognized prior errors ($d=500''$, $l < 20''$), the demodulation performs better than the uniform average, and approaches the flat prior estimate as $l \rightarrow \infty$. The flat prior, in turn, performs better than the uniform average. The solar diameter is $1920''$, so that

$l > 2000''$ effectively represents a trivial prior, which only indicates that the photons came from the sun.

As a practical implication, we learn from Figure 6 (and from similar simulations) that, for realistic uncertainties (say, $d \leq 50''$), demodulation is beneficial compared to the uniform average if $l \gtrsim 10''$, and it is beneficial compared to the flat prior if $l \geq 20''$.

4.6. Example of a solar eruption

A recent solar eruption, to which also Figures 1–2 refer, occurred on February 26, 2004. RHESSI has observed the whole eruption, and Figure 7 shows a part of the impulsive rise phase, where most temporal fine structures are expected. The observed counts of subcollimators (1,3,4,5,6,7,8,9) are divided into disjoint intervals of duration $\tau = 0.12\text{s}$, while subcollimator 2 is rejected due to increased background (Smith et al. 2002). The centroid $\mathbf{x}_0 = (245'', 340'')$ and size $l = 30''$ of the spatial prior are taken from a long-exposure (10s) RHESSI imaging and in agreement with the simulations of Sect. 4.5. The filling factor is assumed to be $\gamma = 0.4$. The average count rate is about 4000 ct/s/subcollimator, and energies from 5 to 15 keV are used.

In order to remove some arbitrariness of the time binning and to assess the quality of the demodulation \hat{b} we proceed as follows. By assumption, the true scene is approximated as piecewise constant in time. If this assumption was true then a second demodulation \hat{b}_{sh} with intervals of equal duration τ but shifted by $\tau/2$ should yield a similar result. By comparing \hat{b} with \hat{b}_{sh} we may thus gain an estimate on the accuracy of the demodulation, and by considering $\hat{b}_{\text{avg}} = \frac{1}{2}(\hat{b} + \hat{b}_{\text{sh}})$ we may remove some arbitrariness of the time binning.

Figure 7 (top panel) shows the estimator \hat{b}_{avg} , together with the uniform average \hat{b}_0 as the simplest possible guess. Panel b) shows the discrepancy between \hat{b} and its time-shifted version \hat{b}_{sh} . As can be seen, the relative discrepancy $|\hat{b} - \hat{b}_{\text{sh}}|/\hat{b}_{\text{avg}}$ is throughout small (6%). The pure Poisson error $\sqrt{\sum_{\mu} c_{\mu} w_{\mu}^2}$ is also shown for comparison (gray line). The residuals $\hat{b} - \hat{b}_{\text{sh}}$ exceed the pure Poisson error, and this excess is due to uncertainties of the weights \mathbf{w} . The latter are caused by the principal reasons discussed in Sect. 4.2, but also have contributions from the uncertainty of the prior centroid \mathbf{x}_0 and -size l , as well as from the approximate form of Equation (1) and its energy-averaged coefficients $\{a_{ni}(t), \psi_i(t)\}$, possible errors of the aspect data $\{\mathbf{P}(t), \arg \mathbf{k}_i(t)\}$, and from violation of the piecewise constant-in-time approximation of the true scene. A complete disentangling of different sources of errors is difficult and somewhat speculative. However, we may empirically compare the residuals $\hat{b} - \hat{b}_{\text{sh}}$ to the residuals $\hat{b}_{\text{avg}} - \hat{b}_{\text{fl}}$ (Fig. 7c) and $\hat{b}_{\text{avg}} - \hat{b}_0$ (Fig. 7d). This shows a clear order of residual amplitudes b) < c) < d), in agreement with the simulations. We may thus be confident that the flat prior estimate improves the uniform average, and that the demodulation improves the flat prior estimate. All residuals are centered about zero, in agreement with unbiasedness. By comparing simulation results with the residuals of Fig. 7 b-d), and with families of similar real-data demodulations with varying τ (not shown), we conclude that the

demodulation error is in the order of the residuals $\hat{b} - \hat{b}_{\text{sh}}$ (Fig. 7b). As may be seen from Figure 7a), many of the excursions of \hat{b}_0 – especially towards low count rates (data gaps) – are absent in \hat{b}_{avg} . They are therefore most likely to be instrumental. Not all of the data gaps can, however, be removed by the demodulation: see, e.g., before 01:53:50. Here, the collective dropout of several detectors during $> \tau$ inhibits successful compensation.

5. Summary

We have developed a unbiased linear Bayes estimator for the photons arriving in front of the RHESSI optics, which applies in situations where imaging information is less in demand than (spatially integrated) temporal evolution. The prior assumptions involve time-independence of the true brightness distribution during $\tau \ll T_S$, and an a gaussian a priori pdf for the source density on the solar disc. The estimator minimizes the expected quadratic deviation of true and retrieved unmodulated counts, while enforcing agreement of their expectation values. Non-overlapping time intervals τ are independent. Geometrically, the algorithm tries to cancel the spatial transmission patterns (modulation patterns) of the RHESSI optics by a suitable linear combination of patterns belonging to the time interval τ . The degree to which canceling is beneficial depends on the counting noise, and the algorithm constructs a trade-off between Poisson- and modulational uncertainties of the estimator. Monte Carlo simulations show that the mean relative error of the demodulation reaches the Poisson limit, and demonstrate robustness against violation of the prior assumptions. An application to a solar eruption is also discussed.

The present method is limited in several ways. First, any non-solar background is neglected. Secondly, the use of sharp time intervals τ brings along the computational advantage that the data can be split and the results merged in the end, but at the cost of possible artifacts at interval boundaries. The use of larger and smoothly tapered time intervals would help, but is computationally demanding.

6. Appendix: Condition number inequalities

The condition number of a positive definite matrix is defined as the ratio of its largest eigenvalue to its smallest eigenvalue. We first ask for simple bounds on the condition number of the matrix $\Lambda_{\mu\nu} = \lambda_\mu \lambda_\nu + \lambda_\mu \delta_{\mu\nu}$ with positive λ_μ . Since Λ is symmetric all its eigenvalues ly between the minimum and maximum of the Rayleigh quotient $R = (\hat{\mathbf{x}}, \Lambda \hat{\mathbf{x}}) = (\hat{\mathbf{x}} \cdot \boldsymbol{\lambda})^2 + \sum_\mu \lambda_\mu \hat{x}_\mu^2$ with $|\hat{\mathbf{x}}|^2 = 1$ (Euclidian norm). The minumum of R is bounded by $R \geq \min(\sum_\mu \lambda_\mu \hat{x}_\mu^2) = \min(\lambda_\mu)$, while the maximum is bounded by $R \leq |\hat{\mathbf{x}}|^2 |\boldsymbol{\lambda}|^2 + \max(\sum_\mu \lambda_\mu \hat{x}_\mu^2) = |\boldsymbol{\lambda}|^2 + \max(\lambda_\mu)$. Therefore, $\text{cond}(\Lambda) \leq (|\boldsymbol{\lambda}|^2 + \max(\lambda_\mu)) / \min(\lambda_\mu)$.

Next we consider the matrix $\mathcal{E}_B \Lambda$. Since it represents an average over different Λ

with different principal directions, we may expect that

$$\text{cond}(\mathcal{E}_B \Lambda) \leq \max_B \text{cond}(\Lambda). \quad (22)$$

To show that this is true it suffices to show that for any two positive definite matrices A_1 and A_2 of equal size the inequality

$$\text{cond}(A_1 + A_2) \leq \max(\text{cond}(A_1), \text{cond}(A_2)) \quad (23)$$

holds. Equation (22) then follows by induction over i with $A_i = dP(B_i)\Lambda(B_i)$. (Assuming that the true scenes may be labeled by discrete labels i . We shall not prove this assertion, but call it plausible in view of the finite resolution of the modulation patterns.) Equation (23) is then easily verified by direct calculation:

$$\begin{aligned} \text{cond}(A_1 + A_2) &= \frac{\max((\hat{\mathbf{x}}, A_1 \hat{\mathbf{x}}) + (\hat{\mathbf{x}}, A_2 \hat{\mathbf{x}}))}{\min((\hat{\mathbf{x}}, A_1 \hat{\mathbf{x}}) + (\hat{\mathbf{x}}, A_2 \hat{\mathbf{x}}))} \\ &\leq \frac{\max(\hat{\mathbf{x}}, A_1 \hat{\mathbf{x}}) + \max(\hat{\mathbf{x}}, A_2 \hat{\mathbf{x}})}{\min(\hat{\mathbf{x}}, A_1 \hat{\mathbf{x}}) + \min(\hat{\mathbf{x}}, A_2 \hat{\mathbf{x}})} \\ &= \frac{\text{cond}(A_1) \min(\hat{\mathbf{x}}, A_1 \hat{\mathbf{x}}) + \text{cond}(A_2) \min(\hat{\mathbf{x}}, A_2 \hat{\mathbf{x}})}{\min(\hat{\mathbf{x}}, A_1 \hat{\mathbf{x}}) + \min(\hat{\mathbf{x}}, A_2 \hat{\mathbf{x}})} \\ &\leq \max(\text{cond}(A_1), \text{cond}(A_2)). \end{aligned}$$

The last line follows by either assuming $\text{cond}(A_1) < \text{cond}(A_2)$ or $\text{cond}(A_1) > \text{cond}(A_2)$.

The author thanks G. Hurford, A. Csillaghy, R. Schwartz, A. Benz, C. Wigger, P. StHilaire and E. Kirk for helpful discussions and comments.

- Aschwanden M J, Benz A O and Schwartz R 1993 *ApJ*, **417** 790
 Byrne C Houghton D and Jiang T 1993 *Inverse Problems* **9** 39
 Dennis B 1985 *Solar Phys.* **100** 465
 Evans S N and Stark P B 2002 *Inverse Problems* **18** R55
 Fivian M and Zehnder A 2002 *Solar Phys.* **210** 87
 Golub G H and Van Loan C F 1989 *Matrix Computations* John Hopkins Univ. Press, Baltimore
 Hurford G G et al. 2002a *Solar Phys.* **210** 61
 Hurford G G and D W Curtis 2002b *Solar Phys.* **210** 101
 Lin R et al 2002 *Solar Phys.* **210** 2
 Machado M E, Ong K, Emslie A G, Fishman G J, Meegan C, Wilson R and Paciesas W S 1993 *Adv. Space Res.* **123** 183
 Press W H, Teukolsky S A Vetterling W T and Flannery B P 1998 *Numerical recipes in C*, 2nd edition, Cambridge Univ. Press
 Prince T A, Hurford G J Hudson H S and Cranell C J 1988 *Solar Phys.* **118** 269
 Rybicki G B and Press W H 1992 *Astrophys. J.* **398** 169
 Schnopper H W, Thompson R I, and S Watt 1968 *Space Sci. Rev.* **8** 534
 Skinner G K 1997 *J. British Interplanetary Soc.* **32** 77
 Skinner G K and T J Ponman 1995 *Inverse Problems* **10** 655
 Smith D et al. 2002 *Solar Phys.* **210** 33
 Willmore A P 1970 *Mon. Not. R. astr. Soc.* **147** 387
 Zehnder et al 2003 *Proceedings of the SPIE* **4853** 41

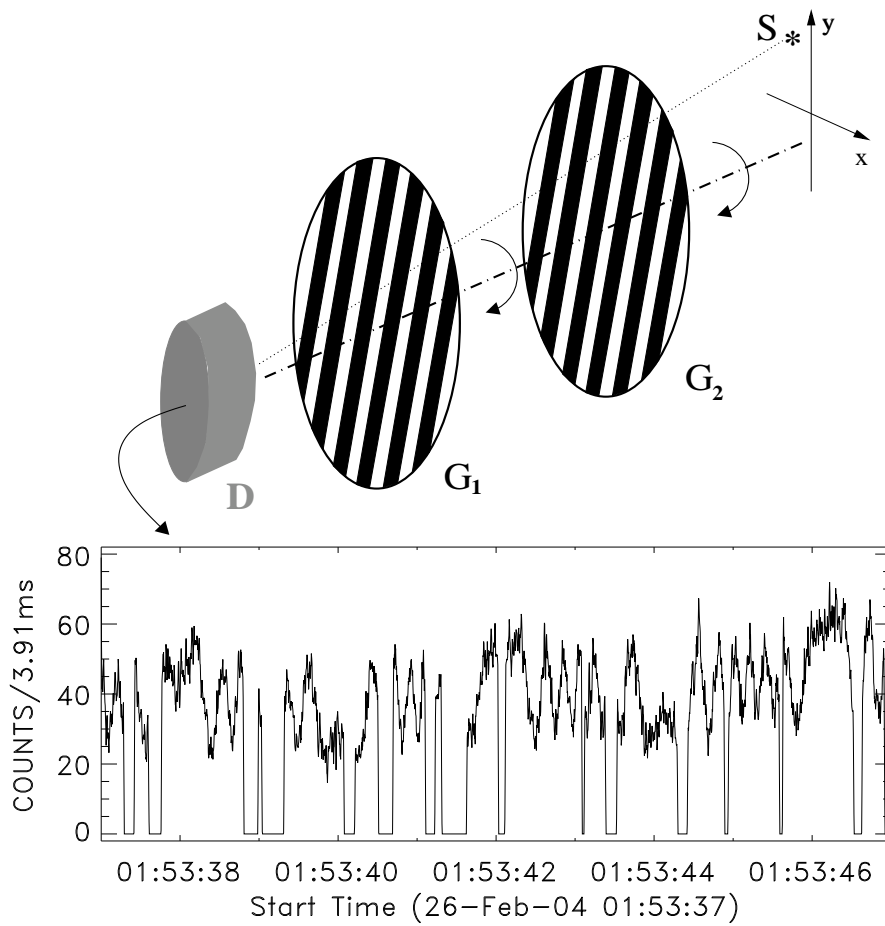


Figure 1. Rotation modulation observing principle. Top: the probability that a photon emitted by the source (S) reaches the detector (D) is diminished if its path (dotted) penetrates the bars (black) of the grids (G_1, G_2). As the grids rotate, the source is periodically shadowed and released, so that the observed flux exhibits characteristic modulations (bottom), from which the true scene in the solar plane (x, y) can be recovered. The RHESSI instrument has 9 pairs of grids ('subcollimators'), of which only #6 is shown. Times with zero count rates represent data gaps.

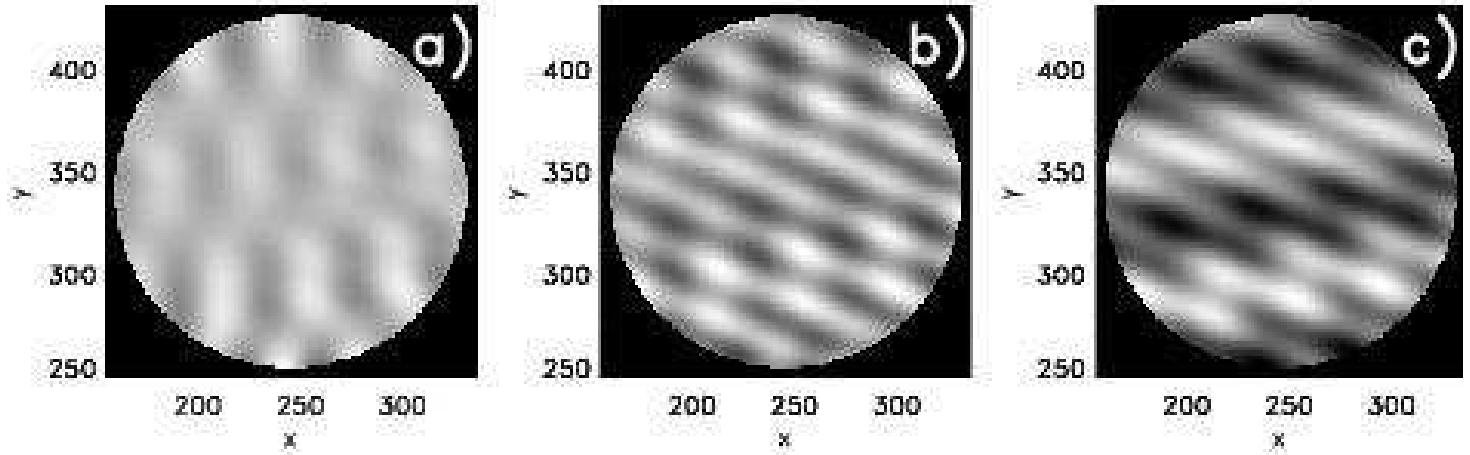


Figure 2. The function $\Phi(\mathbf{x})$ obtained from subcollimators (3,4,5,6) and time interval $\tau=0.2\text{s}$ starting at Feb. 26 2004, 01:53:39.850 UT. a) for infinite count rate ($\Delta\Phi/\Phi=0.0058$); b) adapted to the actual count rate ($\Delta\Phi/\Phi=0.024$); c) in the limit of zero count rate ($\Delta\Phi/\Phi=0.14$). For $\Delta\Phi/\Phi \rightarrow 0$ the effect of modulation is canceled. See text.

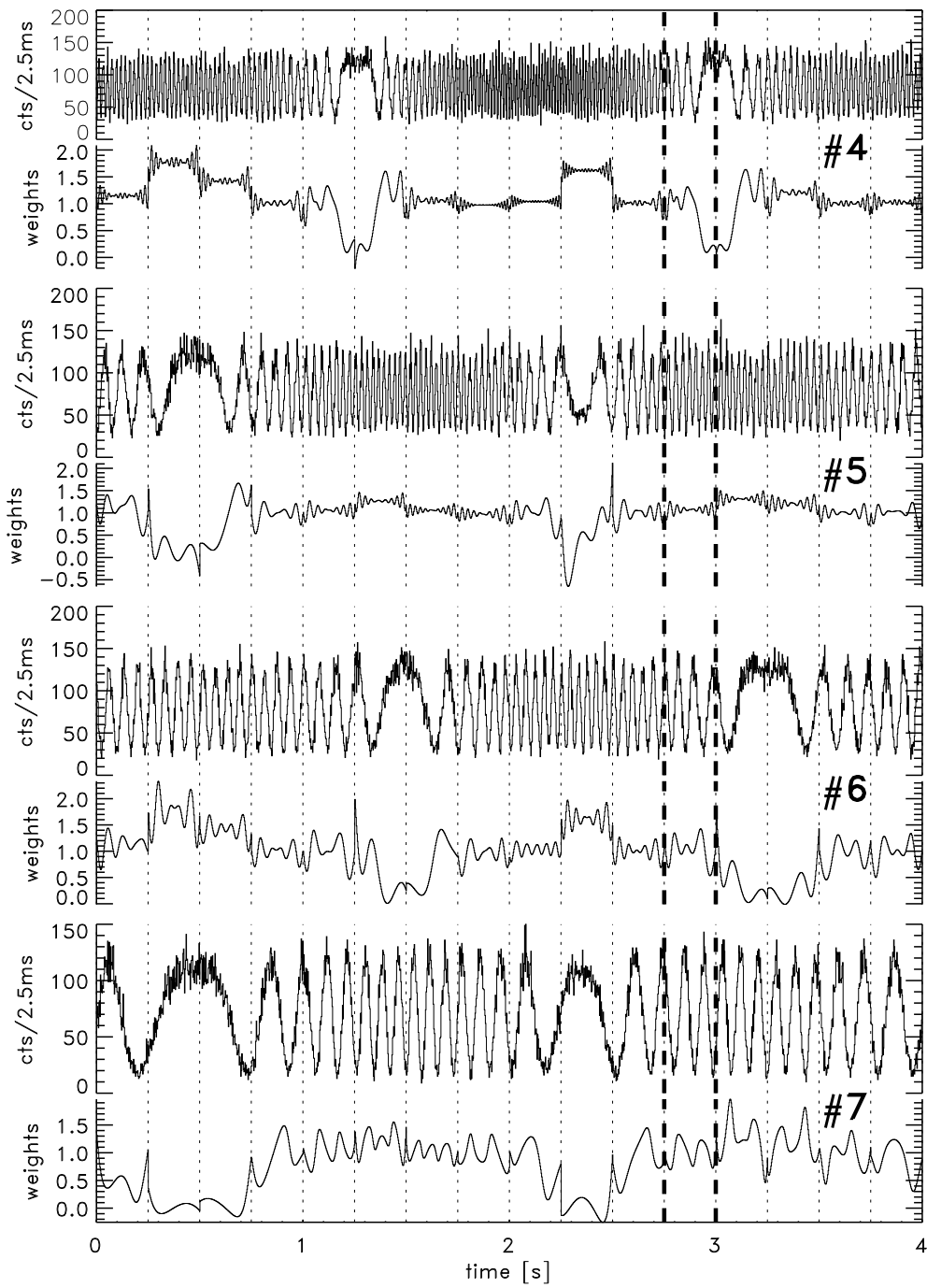


Figure 3. Simulated example of binned count rates and corresponding weights in disjoint intervals (dotted). The boldface dashed interval refers to Fig. 4. See text.

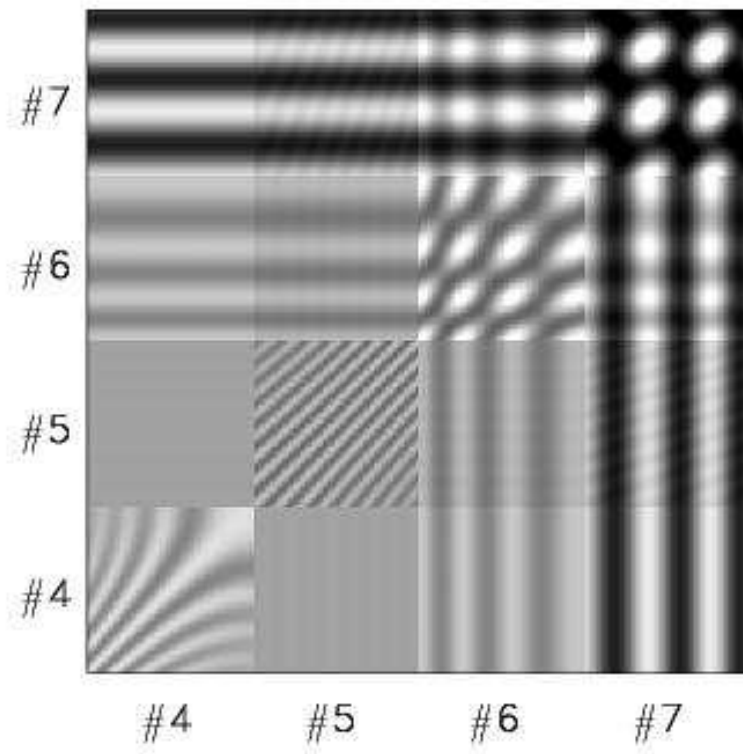


Figure 4. Correlation $\langle M_\mu M_\nu \rangle$ for $2.75s \leq t \leq 3s$ in Fig. 3. Diagonal blocks contain the temporal autocorrelations of the 4 subcollimators, with time running from left to right.

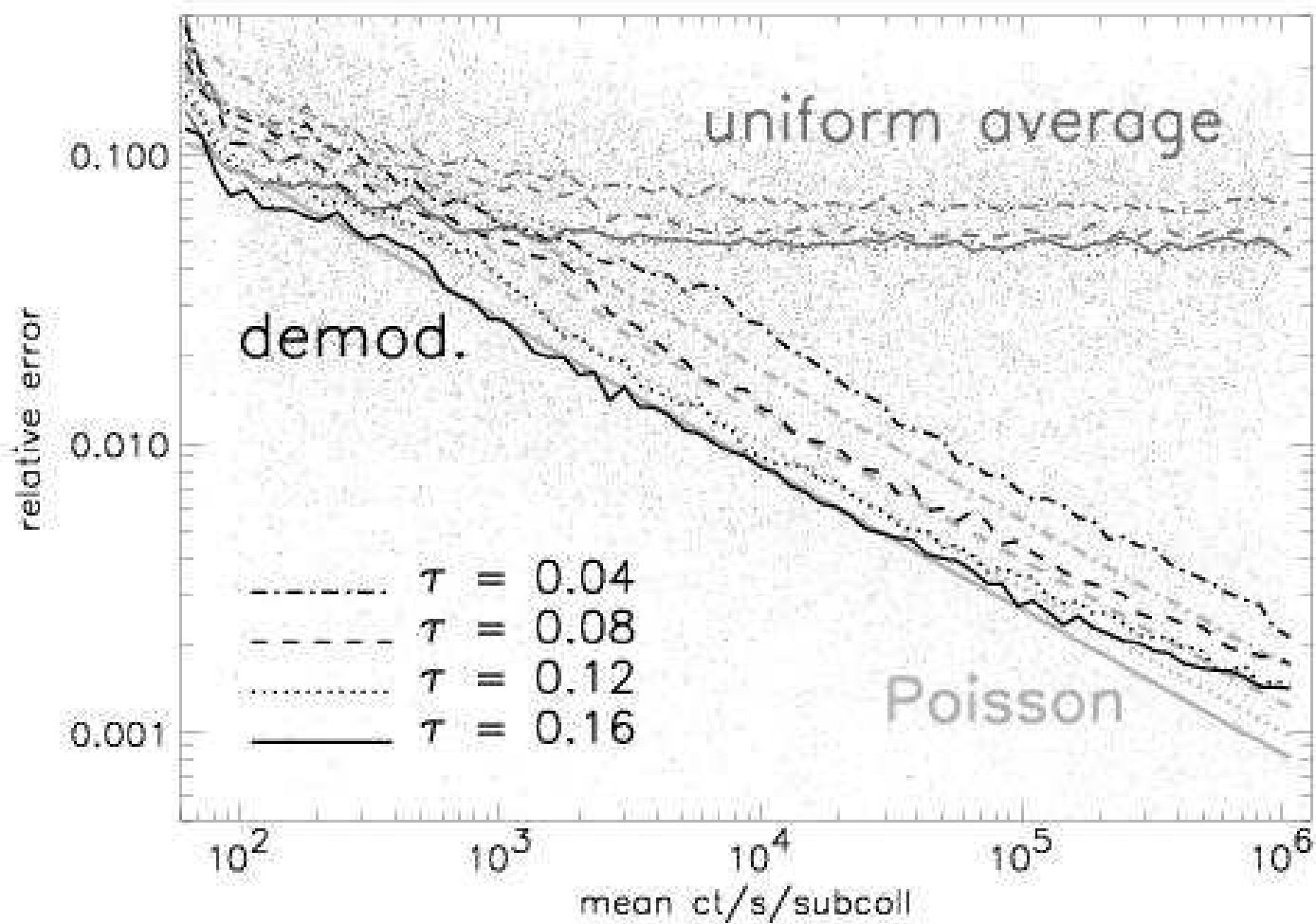


Figure 5. Simulated relative errors of demodulation, uniform average, and the Poisson limit. The curves represent averages over 10^5 samples, some of which are shown as dots. All subcollimators are used, $\gamma = 0.1$, and $l = 40''$. A color rendering of this figure is available in the online version.

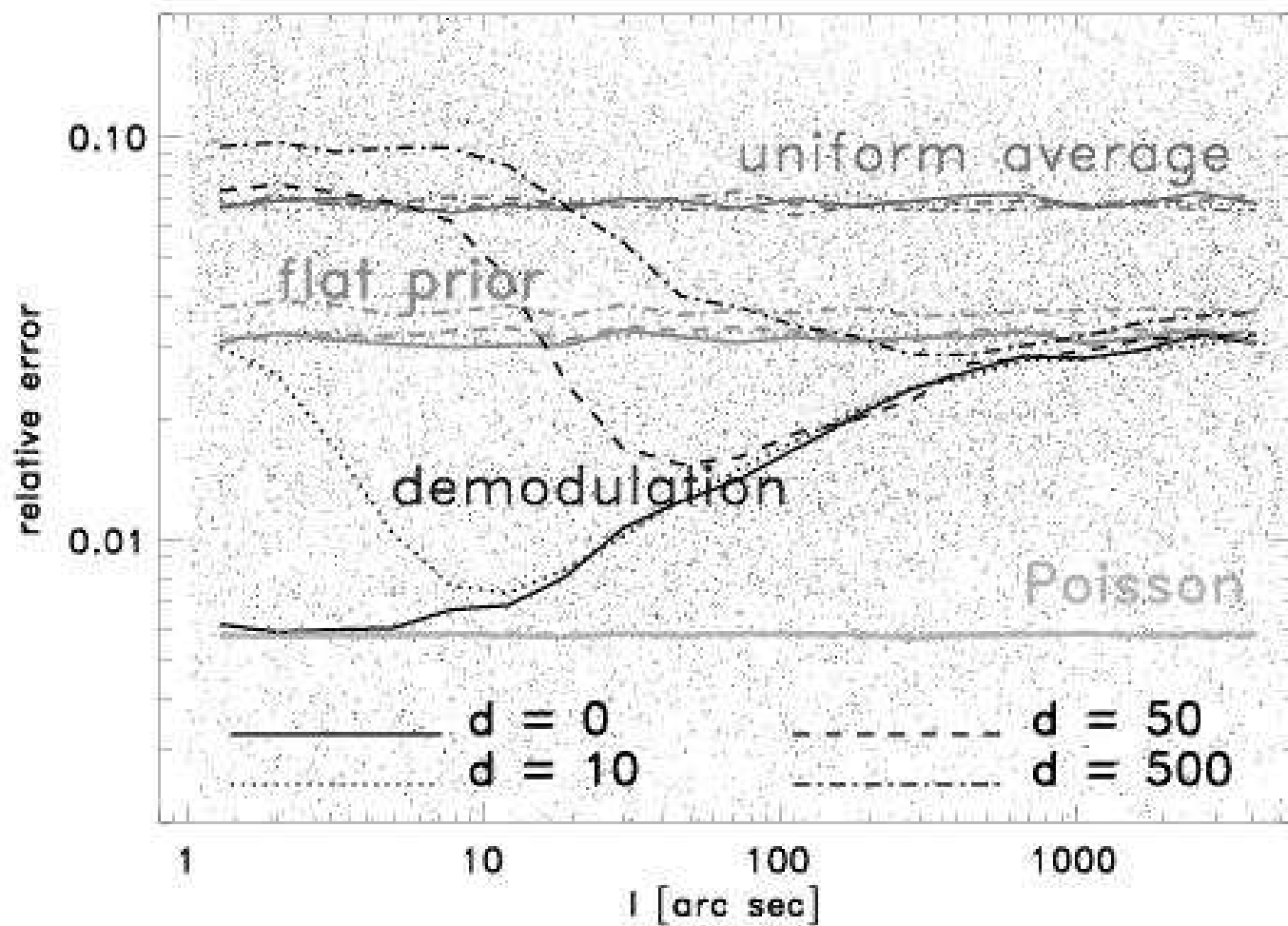


Figure 6. Influence of the prior on the demodulation. The true source is d arc seconds away from the prior centroid. The simulation explores different prior sizes l at fixed count rate $2 \cdot 10^4$ ct/s/subcollimator and time interval $\tau = 0.12$ s, and displays relative errors similar as in Fig. 5. The ‘demodulation’ is given by Eq. (10); the ‘uniform average’ by Eq. (20); the ‘flat prior’ by Eq. (21). A color rendering of this figure is available in the online version.

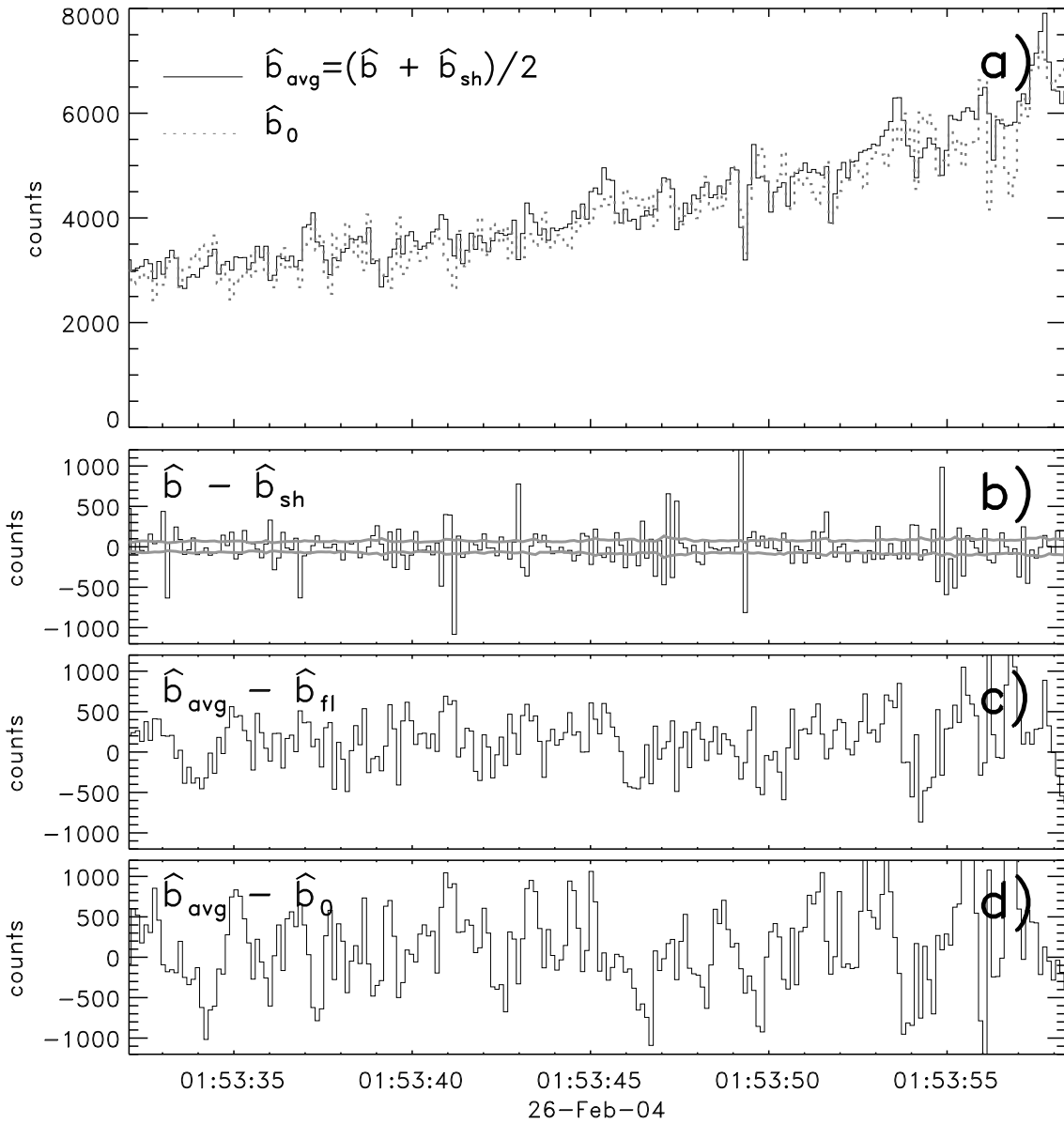


Figure 7. Real-data application of demodulation. a) demodulation (solid) and uniform average (dotted) of subcollimators (1,3,4,5,6,7,8,9) and $\tau = 0.12\text{s}$. The demodulation \hat{b}_{avg} is an average over two solutions \hat{b} and \hat{b}_{sh} (Eqns. 4, 10) which differ only by an offset $\tau/2$ of the time intervals. b) discrepancy of the two solutions, together with the pure Poisson error (gray line). c) residuals between \hat{b}_{avg} and the flat prior estimate \hat{b}_{fl} (Eq. 21). d) residuals between \hat{b}_{avg} and the uniform average \hat{b}_0 (Eq. 20).